

Drag reduction of circular cylinders by porous coating on the leeward side

Katharina Klausmann^{1,†} and Bodo Ruck¹

¹Laboratory of Building- and Environmental Aerodynamics, Institute for Hydromechanics,
Karlsruhe Institute of Technology, Kaiserstrasse 12, 76131 Karlsruhe, Germany

(Received 21 December 2015; revised 4 November 2016; accepted 8 November 2016;
first published online 19 January 2017)

The present paper describes the effect of drag reduction of circular cylinders due to a porous coating on their leeward sides. To investigate the coating effect, experiments were conducted in a wind tunnel of Goettingen type. Systematic drag measurements were carried out for different cylinder configurations and flow velocities. The drag measurements were complemented by pressure and particle image velocimetry (PIV) flow field measurements around selected cylinders. The Reynolds numbers were varied in the subcritical range of $3 \times 10^4 < Re < 1.4 \times 10^5$. The results show that a thin porous layer on the leeward side, either incorporated in the cylinder shape or applied on the cylinder surface, leads to an increase of base pressure on the leeward side of the cylinder. It causes a reduction of drag and dampens oscillation amplitudes when compared to a cylinder without coating. Results obtained for different configurations with varying key parameters (coating angles, layer thicknesses and pore sizes of the porous material) clearly indicate the drag-reducing and amplitude-damping potential of leeward coating. The amount of drag reduction and amplitude damping depends on the combination of key parameters. It was demonstrated that the lowered drag coefficients c_d were almost constant in the tested range of Reynolds numbers. A maximum reduction of drag of 13.2 % was measured. In addition, the results revealed a strong reduction of the pressure fluctuations around cylinders with a leeward coating due to the shift of the vortex region further downstream.

Key words: drag reduction, flow–structure interactions, porous media

1. Introduction

The reduction of drag forces acting on bluff bodies is of great technical importance. Application of drag-reducing techniques can play a crucial role in saving energy for locomotion, damping of oscillations, material fatigue of construction elements, preventing destructive resonance-type oscillations of structures or noise reduction in machinery. Drag of bluff bodies can be reduced by active or passive flow control methods, as was shown by many previous numerical and experimental studies. Typical active control methods, see also reviews of Choi, Jeon & Kim (2008) and Perlin & Ceccio (2015), are based on discrete oscillations of bluff bodies (Cetiner & Rockwell 2001; Carberry, Sheridan & Rockwell 2005), polymer injection (Lumley 1969; Hoyt

† Email address for correspondence: katharina.klausmann@kit.edu

1972), bubble/gas injection (Merkle & Deutsch 1992; Lin, Towfighi & Rockwell 1995; Ceccio 2010), fluid suction (Ackeret 1926; Schlichting 1948; Fransson, Konieczny & Alfredsson 2004) or plasma-based devices (Moreau 2007; Choi, Jukes & Whalley 2011). Typical passive control devices are based on surface modification by roughness, textures, patterns, longitudinal grooves or dimples (Achenbach 1971; Shih *et al.* 1993; Bechert & Hoppe 1985; Frohnäpfel, Jovanović & Delgado 2007; Bearman & Harvey 1993; Choi, Jeon & Choi 2006). Besides homogeneous surface modifications, local components like tripping wires can also be used to trigger the transition of the boundary layer from the laminar to turbulent state and to reduce drag, see Wieselsberger (1913), Fage & Warsap (1929) or James & Truong (1972). Another type of passive control techniques uses permeable coatings, covers, sheaths and shrouds. Price (1956) and Wong (1979) reported a delay in vortex formation and a suppression of vibration of shrouded cylindrical pillars as a result of slats. According to Price (1956) vibration suppression is induced by the delay in vortex street formation. This is obvious from the visualisation study of Galbraith (1980), who analysed the flow pattern around a shrouded cylinder at Reynolds number $Re = 5 \times 10^3$ and reported a significant base bleed. He concluded that the bigger the amount of base bleed is, the longer the vortices take to form and the lower is the drag, see also Galbraith (1981). This seems to hold not only for permeable shrouds, but also for highly porous permeable homogeneous surface layers as those presented in this paper.

Whereas boundary layer flows at flat porous medium/fluid interfaces have been investigated by several authors see e.g. Zagni & Smith (1976), Kong & Schetz (1982), Zippe & Graf (1983), Vafai & Thiyagaraja (1987), Hahn, Je & Choi (2002), Breugem, Boersma & Uittenbogaard (2006), the combination of shaped or bluff bodies (with non-zero pressure gradients) and partial porous coatings has not yet been investigated sufficiently. Partial coating of bluff bodies with porous materials could reduce energy consumption, as was stated by Bruneau, Mortazavi & Gilliéron (2006), who carried out a numerical simulation and found that flow resistance of vehicles could be reduced by up to 45 %. Other numerical simulations indicated that the amplitude due to vortex shedding, which may lead to destructive structure oscillations, can be reduced by applying a porous outer layer (sheath) on the body, see Bruneau & Mortazavi (2006) and also Bhattacharyya & Singh (2011). The few existing, mainly numerical studies suggest that interfacial effects of porous walls can be used to reduce drag of bodies submersed in a flow. Partial coating of bluff bodies with highly permeable porous media seems to open up new possibilities of passive flow control. However, it is not known and not fully understood how partial porous coating changes the fluid mechanical properties of the coated body. This even holds for simple geometries, i.e. flow around circular cylinders or spheres with partial porous surface coatings. Computation of flow over and through porous media still is a challenge, in particular for high Reynolds numbers, see Moessner & Radespiel (2015). The few existing studies are of numerical nature and subject to well-known limitations of resolution and representation of rather complex and dominating interfacial effects. Experimental investigations contributing to the fundamental understanding of the phenomena involved are lacking.

In the investigation reported here, highly permeable foam material was used with isotropic porosity. The medium was equally permeable in three directions, which made it differ from most porous surfaces of hole-based or perforated one-dimensional porosity used in past technical applications. As a consequence, a boundary layer can exist within the material. Beavers & Joseph (1967) made one of the first experimental investigations of flow over and through a three-dimensional permeable block and

found a boundary layer region within their porous material. Furthermore, a numerical simulation by de Lemos (2005) and de Lemos & Silva (2006) revealed that fluxes of momentum and turbulent kinetic energy penetrated the interface between a turbulent flow and a highly porous layer. Apparently, flow over a wall with highly porous coating can be subdivided into different layers. Bruneau & Mortazavi (2008) presented a complex subdivision into five different zones: (i) a boundary layer inside the porous medium close to the impermeable wall, (ii) a region of almost homogeneous flow inside the porous medium, (iii) a zone of velocity increase in the porous medium to reach the free flow velocity at the interface between porous medium and free flow, (iv) the fluid boundary layer at the interface with the free flow and (v) the outer flow zone.

In this paper, a circular cylinder was chosen as a typical bluff body geometry, which is widespread in use, well known and investigated best with respect to its fluid mechanical properties. Historically, this geometry is connected with the names of Strouhal (1878), von Kármán (1911), Wieselsberger (1921) and Roshko (1961), see also reviews of Hoerner (1965) and Zdravkovich (1997, 2003). A porous layer (three-dimensional permeable polyester foam with controlled pore spacings) was used on the leeward side of the cylinder as a passive control device. The leeward side was chosen because preliminary studies with fully porous coated cylinders have revealed an increase in drag. Flow around different cylinder configurations with varying coating angles, varying layer thicknesses and varying pore sizes of the porous foam material was studied fundamentally. The investigations were carried out by the Laboratory of Building and Environmental Aerodynamics of Karlsruhe Institute of Technology (KIT). The aim was to contribute to the understanding of drag reduction of cylinders by leeward coating with porous layers.

2. Experimental details

2.1. Wind tunnel

Systematic drag force measurements were performed in a wind tunnel of Goettingen type for different cylinder configurations. The working cross-section downstream of the nozzle was 75 cm × 75 cm. For the diameter of the cylinder ($D_{cyl} = 7$ cm), Reynolds numbers ranged from 3.5×10^4 to 1.4×10^5 . This corresponded to a velocity range from 8 m s^{-1} to 28 m s^{-1} . During the drag measurements, the velocity was controlled by a Prandtl tube installed upstream of the test section. Precise laser-Doppler anemometry (LDA) measurements revealed that the approaching flow was uniform in vertical and horizontal direction (top-hat profile) and turbulence intensity was less than 1 %. Figure 1 shows the horizontal velocity profiles in the wind tunnel cross-section for four mean velocity variations (from 8.45 m s^{-1} to 11.45 m s^{-1}), measured at a distance of three cylinder diameters upstream of the cylinder's test position.

2.2. Cylinders with integrated porous layer

The cylinders consisted of balsa wood and had a precise and constant outer diameter of $D_{cyl} = 7$ cm, a length of $L_{cyl} = 70$ cm and a smooth surface. The cylinders were placed horizontally in the test section, see figure 1. A porous layer of polyester foam material was inserted on the leeward side of the cylinders. It was symmetrical to the horizontal stagnation line. Four different cylinder configurations with coating angles of $\beta = 40^\circ$, $\beta = 70^\circ$, $\beta = 100^\circ$, $\beta = 160^\circ$ were used for the force measurements,

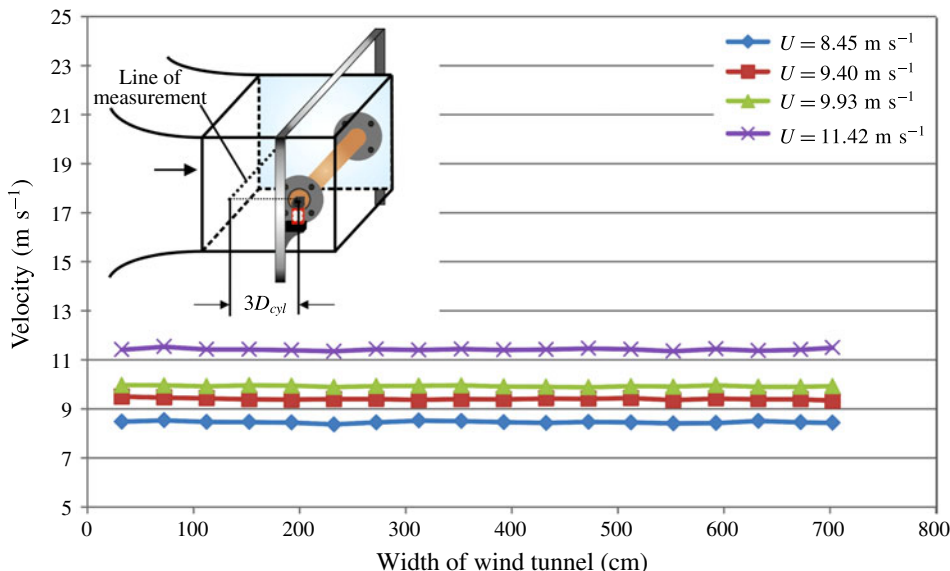


FIGURE 1. (Colour online) Horizontal velocity profile $3D_{cyl}$ upstream of cylinder position, measured by LDA without test cylinder.

Coating angle β (deg.)	Layer thickness d_M (mm)	Porosity (PPI)
40*	3, 5, 10*	10*, 20, 30
70	3, 5, 10	10, 20, 30
<u>100</u> *	3, 5, <u>10</u> *	<u>10</u> , <u>20</u> , <u>30</u>
160	3, 5, 10	10, 20, 30

TABLE 1. Configurations of cylinders with partial porous coating (force measurements). Pressure measurements were performed for underlined configurations. For the asterisked configurations particle image velocimetry (PIV) measurements were performed.

see table 1. For each angle configuration, three different layer thicknesses ($d_M = 3, 5, 10 \text{ mm}$) and three different porosities of 10, 20, 30 PPI (pores per inch) were investigated, see figure 2. In addition, a non-coated smooth balsa wood cylinder was built and its drag was measured for comparison with results of cylinders with a porous coating on the leeward side.

The fluid mechanical properties of the porous foam material can be defined by the pressure loss coefficient $\lambda (\text{m}^{-1})$:

$$\lambda = \frac{p_{\text{wind}} - p_{\text{lee}}}{0.5\rho U^2 d}. \quad (2.1)$$

It describes the difference between the windward and the leeward pressure of a block of porous foam material filling the cross-section of a test channel divided by the dynamic pressure and the characteristic thickness d of the foam material. For the different foam materials of PPI 10, 20 and 30, λ can be specified as $\lambda_{\text{PPI10}} \approx 250 (\text{m}^{-1})$, $\lambda_{\text{PPI20}} \approx 500 (\text{m}^{-1})$ and $\lambda_{\text{PPI30}} \approx 1000 (\text{m}^{-1})$, respectively.

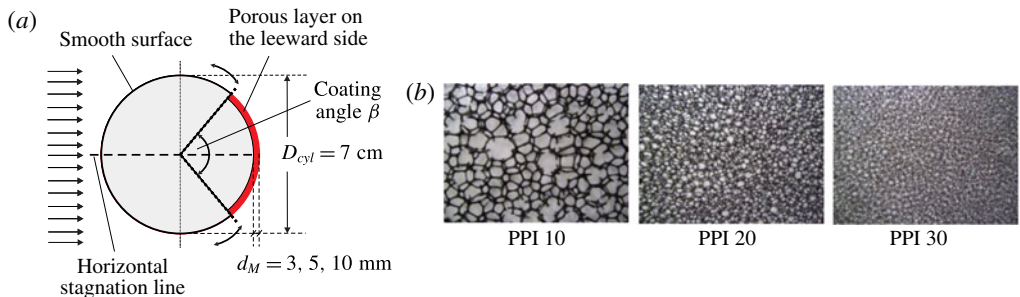


FIGURE 2. (Colour online) Sketch of cylinder configuration with inserted porous layer on the leeward side, which is symmetrical to the horizontal stagnation line (*a*); porous foam material of the three different pore sizes (*b*).

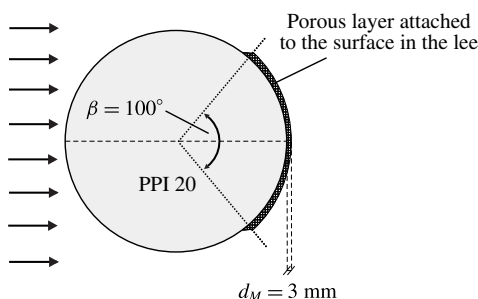


FIGURE 3. Plexiglas cylinder with additional porous layer applied on the leeward side.

2.3. Cylinder with porous layer applied to the surface in the lee

A second type of cylinder model was made. It consisted of a smooth Plexiglas cylinder with the same diameter of $D_{cyl} = 7 \text{ cm}$. On its lee side, a thin porous layer of 3 mm thickness and PPI 20 was not inserted into the cylinder's shape as before, but applied onto the surface. The coating angle was $\beta = 100^\circ$, and the coating was symmetrical to the horizontal stagnation line, see figure 3. To prevent three-dimensional flow conditions at the ends of the cylinders, all configurations were mounted between circular end plates (splitter plates) and fixed to a steel frame outside of the wind tunnel, see figures 4 and 5. The splitter plates were decoupled from the tested cylinders by fitting the models in circular holes of the splitter plates. The diameter of these holes slightly exceeded that of the models. The outer diameter of the splitter plates was $D_{plate} = 3.5 \cdot D_{cyl}$. The splitter plates were designed according to the findings of Stansby (1974) and Szepessy (1993), corresponding to a distance x_l from the leading edge to the cylinder axis of $x_l/D = 1.75$ and a distance x_t from the cylinder axis to the trailing edge $x_t/D = 1.75$. On the wall sides the plates were provided with PVC-caps to prevent gap flow between cylinder model and splitter plates.

2.4. Drag force measurement

Total drag was measured for different flow velocities by a force balance which consisted of two strain gauge sensors. The sensors had a nominal force of 50 N each

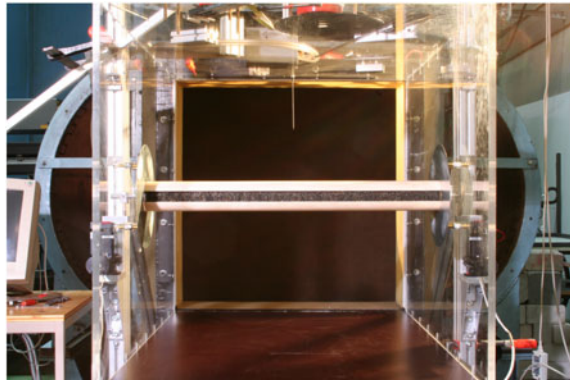


FIGURE 4. (Colour online) Cylinder configuration in the wind tunnel; view in upstream direction.

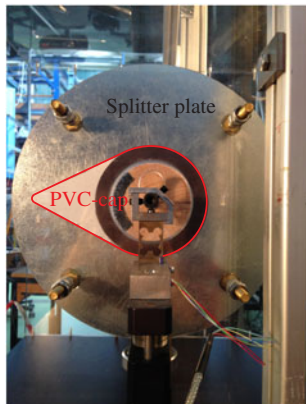


FIGURE 5. (Colour online) Splitter plate with PVC-cap and strain gauge sensor.

and an accuracy of 0.04 %. The cylinder configurations were connected directly to the sensors, which were fixed to the steel frame installed outside, see figures 5 and 6. 20 000 voltage values were recorded at a sampling frequency of 500 Hz for each tested velocity.

The dynamic characteristics of the force balance were determined by measuring the system response over a frequency range of $5 \text{ Hz} \leq f \leq 100 \text{ Hz}$. This was realized by a calibration apparatus which consisted of a mini shaker, a frequency generator and an amplifier. Via the frequency generator sinusoidal signals of different frequencies but with constant amplitude were fed to the shaker as system input. The volt values of the force sensors were taken as output signals of the system. The frequency response of the system with peaking at $f = 28 \text{ Hz}$ is shown in figure 13(c). In addition, a second method – the impulse response method – was also applied and the impulse signal also indicated a peak at about $f = 28 \text{ Hz}$ in the frequency domain. This corresponds to the resonance frequency of the system.

The mean drag force \overline{F}_D can be expressed as the sum of form drag force \overline{F}_p and friction drag force \overline{F}_f :

$$\overline{F}_D = \overline{F}_p + \overline{F}_f. \quad (2.2)$$

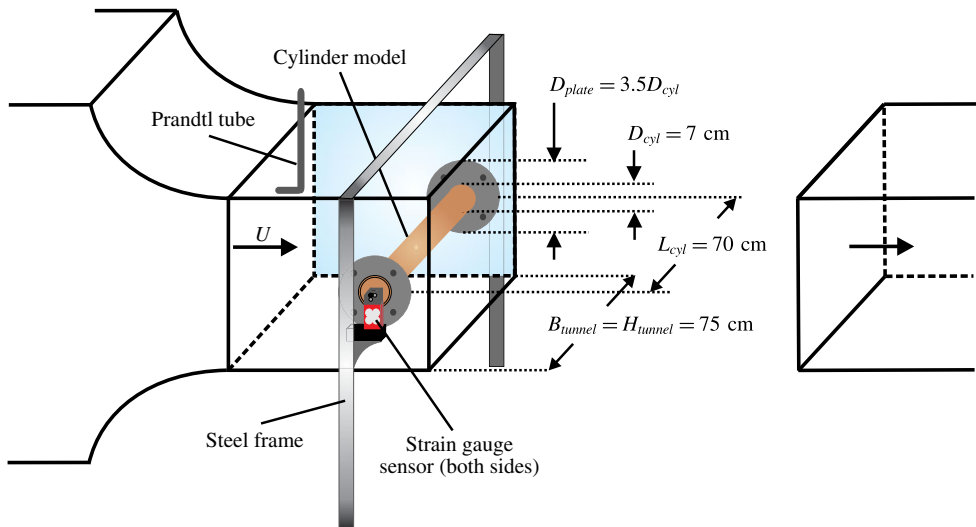


FIGURE 6. (Colour online) Force balance with cylinder configuration installed in the wind tunnel.

Thus, the total drag force can be obtained by summing up all pressure and friction forces acting on the surface elements around the bluff body, which can be expressed by:

$$\overline{F}_D = \int_0^{2\pi} (\bar{p} \cos(\phi) + \bar{\tau}_0 \sin(\phi)) \cdot dA. \quad (2.3)$$

Dividing (2.3) by $1/2 \cdot \rho \cdot U^2 \cdot A$, with $A = L_{cyl} \cdot D_{cyl}$, defines the drag coefficient c_d :

$$\frac{\overline{F}_D}{\frac{1}{2} \rho \cdot U^2 \cdot A} = c_d. \quad (2.4)$$

Especially with respect to similarity, another interesting point is the question regarding on which dimensionless numbers the drag coefficient depends in this particular case. This can be answered by dimensional analysis, where the governing equation is appropriately normalised in order to form dimensionless groups that appear in the resulting dimensionless equation. The mean drag force per unit length of the cylinder \overline{F}'_D obviously depends on the approaching flow velocity U , density of the fluid ρ , dynamic viscosity of the fluid μ , diameter of the cylinder D_{cyl} , pressure loss coefficient of the porous material characterised by the pressure drop per unit length λ and thickness of the porous layer d_M . Thus, the equation can be written as:

$$\overline{F}'_D = f_1(U, \rho, \mu, D_{cyl}, \lambda, d_M). \quad (2.5)$$

Expressing the dimension of each physical quantity in the brackets as a product of the basic physical dimensions and normalizing the quantities n times yield a dimensionless equation, which reads in the present case:

$$\frac{\overline{F}'_D}{\rho \cdot U^2 \cdot D_{cyl}^2} = f_n \left(\frac{\rho \cdot U \cdot D_{cyl}}{\mu}, \frac{\lambda \cdot D_{cyl}}{\rho \cdot U^2}, \frac{d_M}{D_{cyl}} \right). \quad (2.6)$$

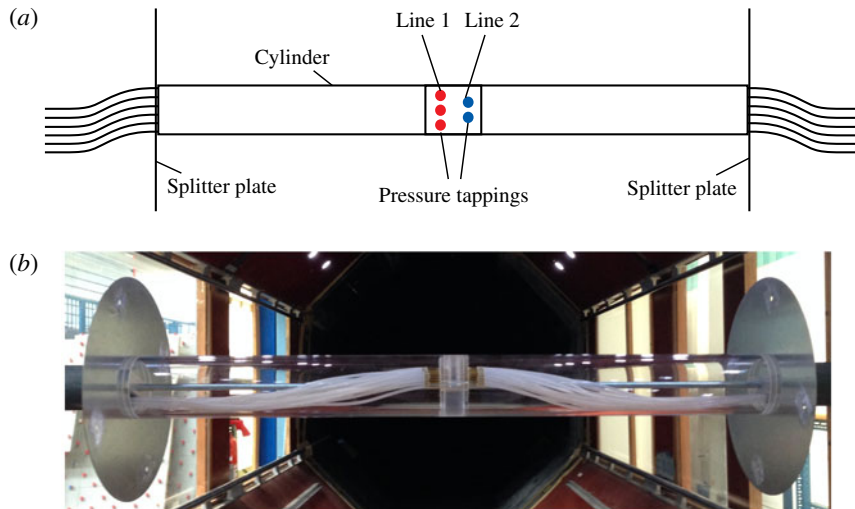


FIGURE 7. (Colour online) Sketch of cylinder model with two lines of pressure tappings in the middle segment (*a*) and photo (*b*); here: smooth cylinder without porous coating.

As can be inferred from (2.6), the first quantity on the right-hand side is the Reynolds number Re and the second is similar to an Euler number Eu describing the ratio of pressure loss in the porous medium to inertia force of the flow. The third quantity reflects the ratio of porous layer thickness to cylinder diameter and accounts for geometrical similarity.

In a wind tunnel having a cross-section of height $H_{tunnel} = 75$ cm, a cylinder with a diameter of $D_{cyl} = 7$ cm mounted perpendicular to the flow direction leads to a blockage of 9.3 %. As a consequence of the blockage effect, flow velocity around the cylinder and, thus, drag measurement must be corrected e.g. according to the image concept of Allen & Vincenti (1944) (used in this study), see also Dalton (1971), or according to the momentum concept of Maskell (1963). Such correction methods consider the change in dynamic pressure caused by the interaction of fixed walls and blocking cylinder, which leads to a wall-wake interference.

2.5. Pressure measurement

For the pressure measurements, cylinder configurations with a coating angle of $\beta = 100^\circ$, $d_M = 10$ mm and foam material of PPI 10, 20 and 30 were investigated, see table 1 underlined. The cylinders were made of smooth Plexiglas and consisted of three segments. The smaller middle segment included the pressure tappings and was fixed between two smooth segments, see figure 7. The pressure tappings were grouped in two lines. The increment between the pressure tappings for each line was 10° . The first pressure tapping of line 1 was placed at the stagnation point ($\phi = 0^\circ$), the last one was at $\phi = 180^\circ$. Line 2 was displaced by 5° and the first tap of this line started at $\phi = 5^\circ$ and ended at $\phi = 175^\circ$. This resulted in a maximum number of 37 pressure tappings on half of the cylinder circumference. In the leeward region, the pressure taps were installed below the porous foam material, see figure 8. To exclude that pressure measurements performed at taps below the porous foam material leads to wrong results, pressure was also measured using tubes that flush with the porous

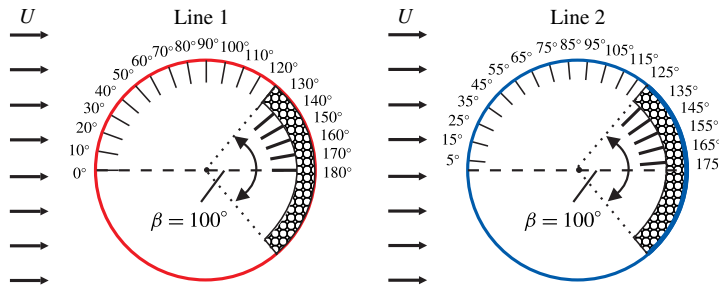


FIGURE 8. (Colour online) Layout of pressure tappings for both lines: configuration PPI 10, $d_M = 10$ mm, $\beta = 100^\circ$.

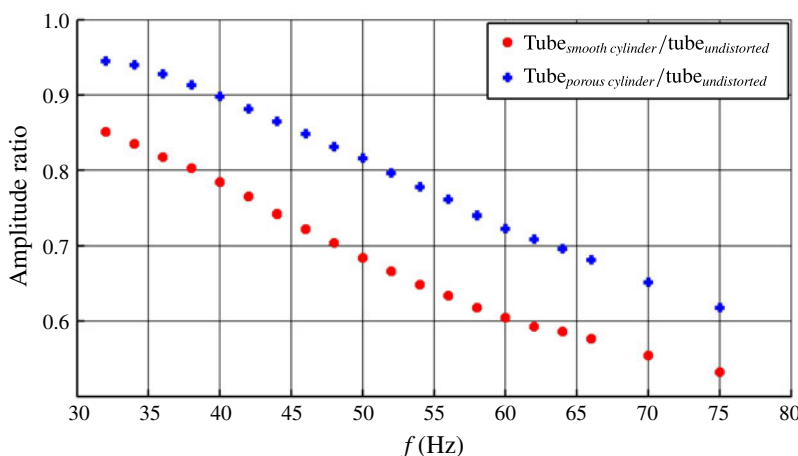


FIGURE 9. (Colour online) Amplitude ratio of the tubing system.

surface, see § 3.5. In order to measure accurately the pressure fluctuations, corrections of distortion effects caused by the tubing system have been performed. This was realized by a calibration apparatus. With a frequency generator and a loudspeaker an acoustical sinusoidal signal was applied simultaneously to port 1 and port 2 of a multiport pressure sensor. The connection from loudspeaker to port 1 was realized by a short tube with a length of $L_{tube} = 2$ cm. This served as corresponding reference pressure of an undistorted signal. The tubing system of the cylinder configuration was interconnected between loudspeaker and port 2. The connection of the corresponding pressure tap to the loudspeaker was also realized by a short tube length ($L_{tube} = 2$ cm). The frequency response was measured within the range of $30 \text{ Hz} \leq f \leq 75 \text{ Hz}$ and is shown in figure 9. The pressure measurements were corrected respectively.

2.6. PIV flow field measurements

The flow field was measured using a DANTEC 2C-2D TR-PIV system for the configurations asterisked, see table 1. The system consisted of double-pulsed Nd:YAG lasers (532 nm) and a high-speed camera with a complementary metal-oxide-semiconductor (CMOS) sensor of 1280×800 pixel resolution. The light sheet was aligned in main stream direction, in the middle of the cylinder configuration. To provide the two-dimensional (2-D) flow and optical accessibility, the cylinder

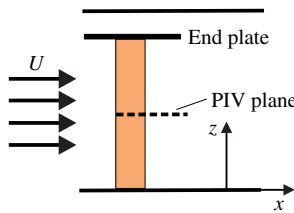


FIGURE 10. (Colour online) PIV plane.

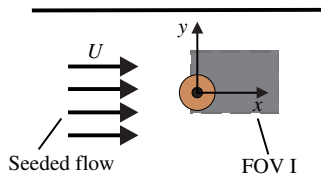


FIGURE 11. (Colour online) Field of view I.

was mounted between the Plexiglas wall on the one side and the splitter plate on the other, see figure 10. PIV data were obtained for the field of view I (FOV I), see figure 11, corresponding to the shear layer and wake regions. The size of the measurement area was 300×185 mm. The images were evaluated using an adaptive correlation algorithm with a final interrogation size of 32×32 pixel by 50 % overlap. The universal outlier detection technique was used to eliminate spurious vectors (DANTEC Software v3.41) based on the work of Westerweel & Scarano (2005). The sampling frequency was $f_{sample} = 1000$ Hz and the total number of images was $N_{images} = 5000$.

3. Results and discussion

3.1. Influence of a porous layer applied to the leeward side of a smooth cylinder

At first, drag measurements were carried out with a fully smooth cylinder made of Plexiglas. Subsequently, a thin porous layer was applied to the leeward side, see figure 3. As can be inferred from figure 12, the applied thin layer causes the drag to be reduced almost constantly in the Reynolds number range. When averaged over the tested Reynolds number range, drag reduction is approximately 9.8 %. This demonstrates the effectiveness of leeward coating as a passive device reducing the drag and influencing the flow field around the coated structure.

In figure 13, a part of the time series of the voltage signal recorded by the force sensors is shown for both configurations, the reference cylinder (figure 13a) and the identical cylinder with the porous layer coating in the lee (figure 13b), respectively. The mean velocity of this experiment was $U = 24.2$ m s⁻¹. The voltage curve can be taken as a measure of the curve of the resulting horizontal wind force acting on the cylinder. The instantaneous force measurements were performed in a velocity/frequency range far away from the system resonance frequency as indicated in the diagram of figure 13(c).

As can be seen, the signal curve of the cylinder with the porous layer coating shows qualitatively a significant reduction in amplitude oscillation and is much smoother

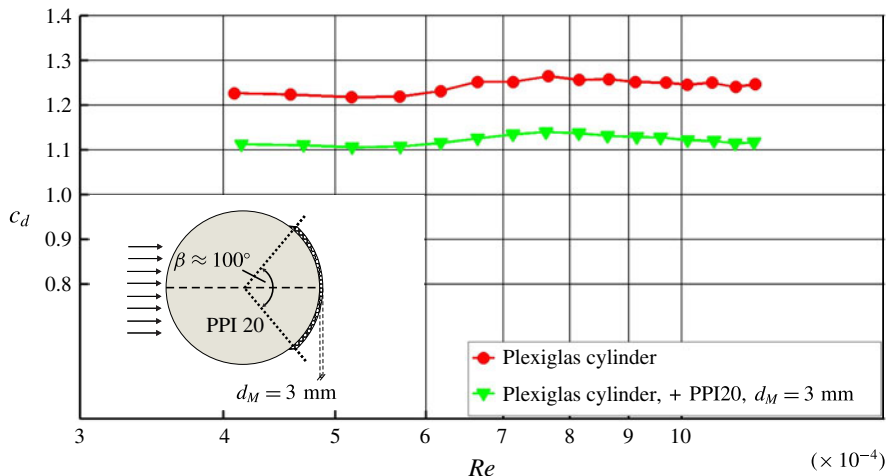


FIGURE 12. (Colour online) Drag coefficient of the configuration with an additional thin porous layer on the leeward side.

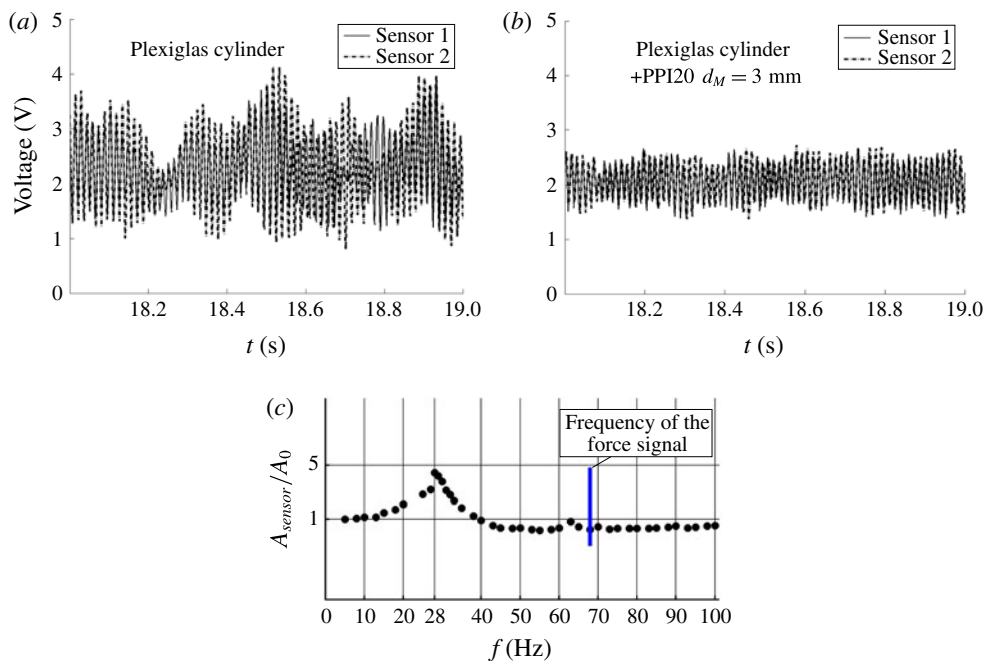


FIGURE 13. (Colour online) (a,b) Time series of voltage data of the force sensors for a smooth Plexiglas cylinder of 7 cm in diameter and $U = 24.2 \text{ m s}^{-1}$ in mean velocity: without any porous layer (a), with porous layer coating on the leeward side (b). (c) Dynamic characteristics of the force balance with Plexiglas cylinder model, measured over a frequency range of $5 \text{ Hz} \leq f \leq 100 \text{ Hz}$.

and more regular. This difference is recorded during the whole sampling time for all velocity settings.

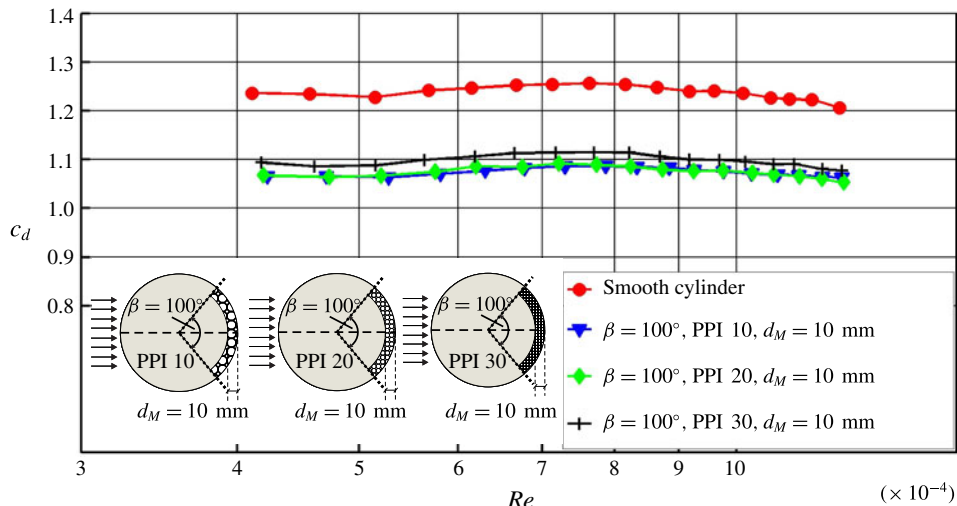


FIGURE 14. (Colour online) Drag coefficient of the cylinder coated on the leeward side with a coating angle of $\beta = 100^\circ$, a constant layer thickness of $d_M = 10$ mm and varying porosity.

Subsection	Coating angle	Porosity	Layer thickness
3.2.1	Constant	Variable	Constant
3.2.2	Constant	Constant	Variable
3.3.1	Variable	Constant	Variable
3.3.2	Variable	Variable	Constant

TABLE 2. Varying parameters.

The results in figures 12 and 13 originate from measurements carried out for verification purposes rather than for obtaining systematic data. Systematic data were obtained using modified cylinder models with shape-integrated porous layers, see figures 2 and 8. As a result, the outer contour of the cylinders was no longer dependent on the layer thickness and remained always constant with a diameter of 7 cm.

3.2. Drag coefficient of cylinders with a coating angle of $\beta = 100^\circ$

Figures 14–17 present the measurement results of the drag coefficient c_d for a coating angle of $\beta = 100^\circ$ and compare them to those of the reference cylinder (smooth cylinder with no porous layer in the lee). The curves of the c_d coefficient are fairly constant over the measured range of Reynolds numbers. The following subsections present the data for varying key parameters, i.e. porosity (pore sizes), porous layer thickness and coating angle. Table 2 gives an overview of the varying parameters.

3.2.1. Constant porous layer thickness

Three different constant layer thicknesses were measured with varying foam material. Exemplarily, it is shown in figure 14 that the variation of porosity has

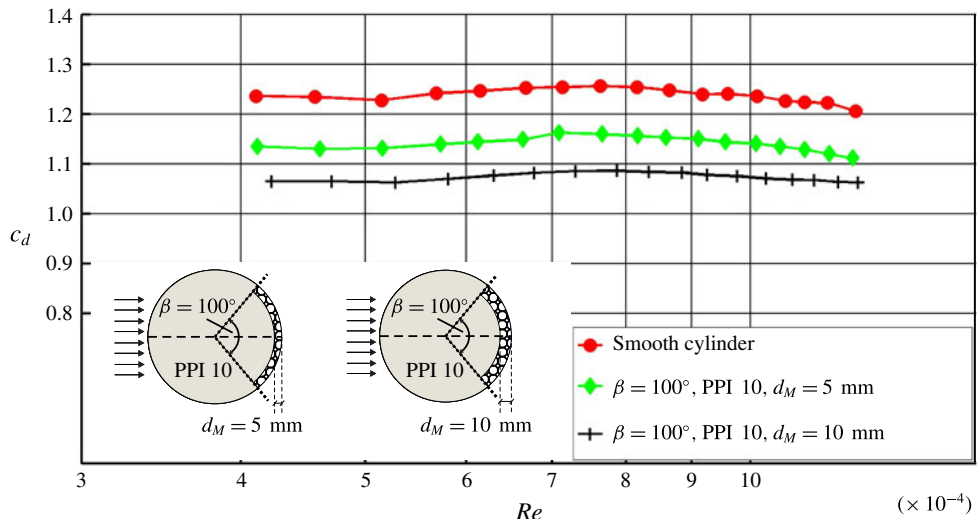


FIGURE 15. (Colour online) Drag coefficient of the cylinder coated on the leeward side with a coating angle of $\beta = 100^\circ$, constant PPI 10 foam material and varying layer thickness.

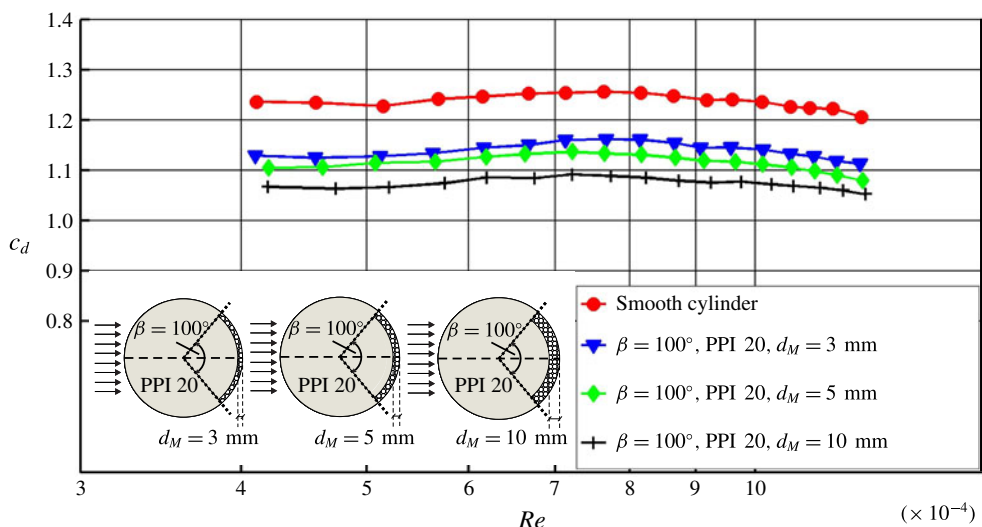


FIGURE 16. (Colour online) Drag coefficient of the cylinder coated on the leeward side with a coating angle of $\beta = 100^\circ$, constant PPI 20 foam material and varying layer thickness.

small influence. In all configurations, the porous coating on the leeward side causes a reduced drag compared to the reference cylinder. All inserted porous layers are most effective and reduce the drag significantly. The foam material with PPI 30 shows a drag reduction which is a bit smaller. The reduction of the mean drag over the measured range of Reynolds numbers for the PPI 30 foam material is approximately 11.2% and almost no difference can be measured between foam materials of PPI 10

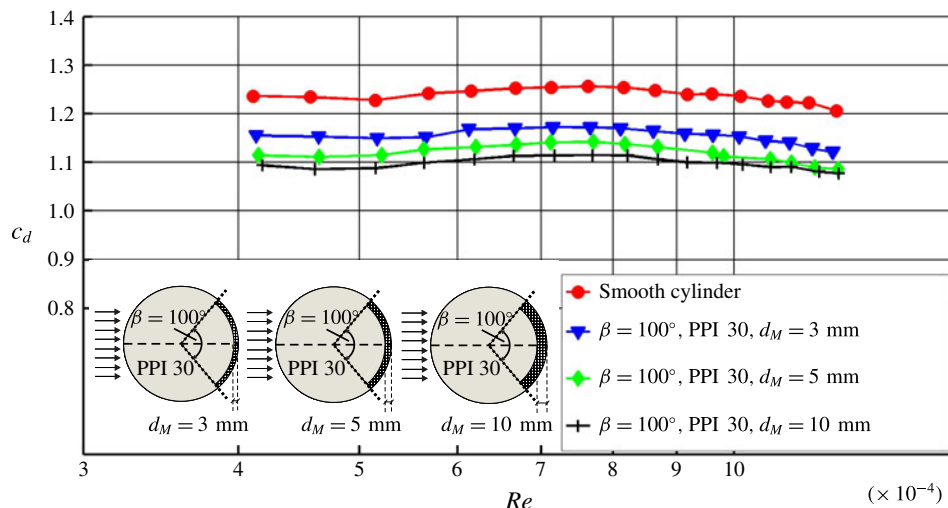


FIGURE 17. (Colour online) Drag coefficient of the cylinder coated on the leeward side with a coating angle of $\beta = 100^\circ$, constant PPI 30 foam material and varying layer thickness.

and PPI 20. For foam materials of PPI 10 and PPI 20 and a layer thickness of $d_M = 10 \text{ mm}$, drag reduction amounts to 13 %. However, the degree of porosity, i.e. the pore size of the foam, does not seem to have the strongest influence on the results.

3.2.2. Constant porosity

The results obtained for porous cylinders coated on the lee with foam material of constant porosity, but varying layer thickness are displayed in figures 15–17. Configurations with a porous coating of PPI 10 foam show a decrease in drag with increasing layer thickness, see figure 15. Compared to the reference cylinder, a drag reduction of 13.2 % results for the porous layer of $d_M = 10 \text{ mm}$ and of 7.7 % for the layer of $d_M = 5 \text{ mm}$. For both foam materials of PPI 20 in figure 16 and PPI 30 in figure 17, the drag reduction effect is almost the same: with increasing layer thickness, drag reduction increases over the measured range of Reynolds numbers. The corresponding curves in figures 15–17 do not deviate very much from each other. In fact, the deviation of the curves obtained for a constant layer thickness, but different layer porosities is approximately 2–3 %, which again shows that the degree of porosity of the foam material seems to be of secondary importance.

3.3. Drag coefficient averaged over the measured Reynolds number range for varying coating angles β

As can be seen from figures 14–17, the drag reduction reached for a cylinder/porous layer combination is almost constant in the measured Reynolds number range (horizontal c_d -curve before the drag crisis). The constancy is found similar to the curve of the reference (smooth) cylinder and is due to the fact that this subcritical Reynolds number range characterized by a laminar boundary layer, periodic vortex shedding and a turbulent wake shows rather stable separation conditions. This allows

Configuration $\beta = 100^\circ$	\bar{c}_d	Deviation from reference cylinder (%)
Reference cylinder	1.24	—
PPI 10, $d_M = 5$ mm	1.14	7.7
PPI 10, $d_M = 10$ mm	1.07	13.2
PPI 20, $d_M = 3$ mm	1.14	7.8
PPI 20, $d_M = 5$ mm	1.12	9.8
PPI 20, $d_M = 10$ mm	1.07	13.1
PPI 30, $d_M = 3$ mm	1.15	6.6
PPI 30, $d_M = 5$ mm	1.11	9.5
PPI 30, $d_M = 10$ mm	1.09	11.2

TABLE 3. Drag coefficient averaged over the measured range of Reynolds numbers and deviation from the reference cylinder drag value for the $\beta = 100^\circ$ configuration.

for the averaging of the drag coefficients in that range and the determination of its deviation from the reference cylinder data, see table 3. Thus, the measured curve of drag coefficients shrinks to a single value. The *Re*-averaged drag \bar{c}_d over the measured velocity range (U_i , with $i = 1\text{--}17$ velocities) is determined by:

$$\bar{c}_d = \frac{1}{n} \sum_{u_i=1}^n c_{d_i}. \quad (3.1)$$

Deviation from the *Re*-averaged reference cylinder value can be written as:

$$\Delta \bar{c}_d = \frac{\bar{c}_{d,config} - \bar{c}_{d,ref}}{\bar{c}_{d,ref}} \cdot 100 \text{ } (\%). \quad (3.2)$$

The curves of measured drag coefficients displayed above refer to a fixed coating angle of $\beta = 100^\circ$. In fact, not only this coating angle was investigated but also other coating angles in the range of $\beta = 40^\circ\text{--}160^\circ$. Using the *Re*-averaged drag coefficients makes it easy to display the measured curves as points in a plot and to accommodate many configurations therein. In figure 18(a–c) the *Re*-averaged drag coefficient is plotted over the coating angles of $\beta = 40^\circ, 70^\circ, 100^\circ$ and 160° for a constant porosity. Figure 19(a–c) shows the drag coefficient over the same coating angles, but for a constant porous layer thickness. The drag coefficient for the coating angle $\beta = 0^\circ$ corresponds to that of the smooth reference cylinder without any coating.

3.3.1. Constant porosity with varying coating angle and varying layer thickness

As can be seen in figure 18, a clear tendency exists for all coating angles investigated: the thicker the layer is, the higher is the reduction of the drag coefficient \bar{c}_d . However, the difference in \bar{c}_d between the three thicknesses depends on the coating angle. The highest reduction in \bar{c}_d can be found for a coating angle of $\beta \geq 100^\circ$. As can be seen from figure 18(a–c), a coating angle of $\beta = 40^\circ$ already reduces \bar{c}_d compared to the reference cylinder ($\beta = 0^\circ$). However, the layer thickness does not seem to be effective at a coating angle of $\beta = 40^\circ$. Almost all values coincide for this angle irrespective of layer thickness. Significant differences in drag coefficient \bar{c}_d are caused by layer thickness variation at coating angles $\beta \geq 70^\circ$. Comparing the results in figure 18(a) shows that for a coating angle of $\beta = 160^\circ$, the \bar{c}_d values for

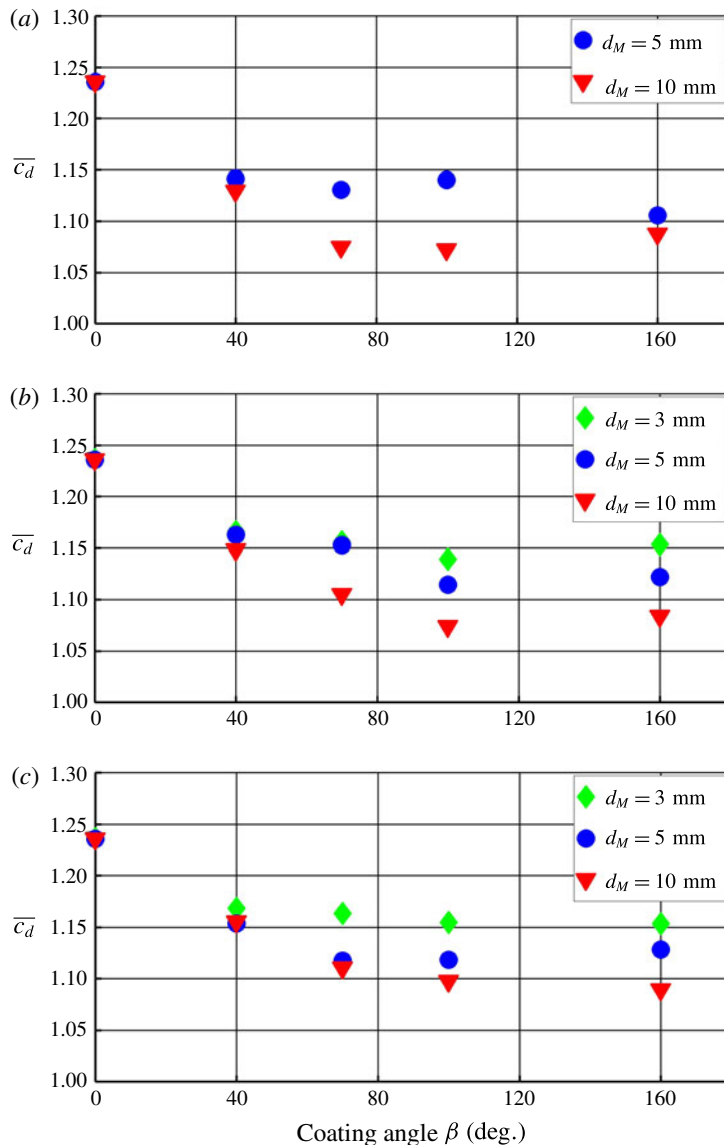


FIGURE 18. (Colour online) Drag coefficient $\overline{c_d}$ with constant porosity over varying coating angle (a) PPI 10, (b) PPI 20, (c) PPI 30.

the two different layer thicknesses ($d_M = 5$ mm and $d_M = 10$ mm) seem to converge to a similar small difference as for coating angle $\beta = 40^\circ$. Apparently, layer thickness variation seems to lose its influence for coating angles $\beta \geq 160^\circ$ at this porosity. This is contrary to the results in figure 18(b,c), where pronounced differences in drag reduction exist for $\beta = 160^\circ$ and different layer thicknesses. Nevertheless, the results in figure 18 show that the variation of coating angle and layer thickness is of primary importance. In this context, it should be noted that the experiments were carried out for selected coating angles ($\beta = 40^\circ, 70^\circ, 100^\circ$ and 160°), which means that the findings refer only to these angles.

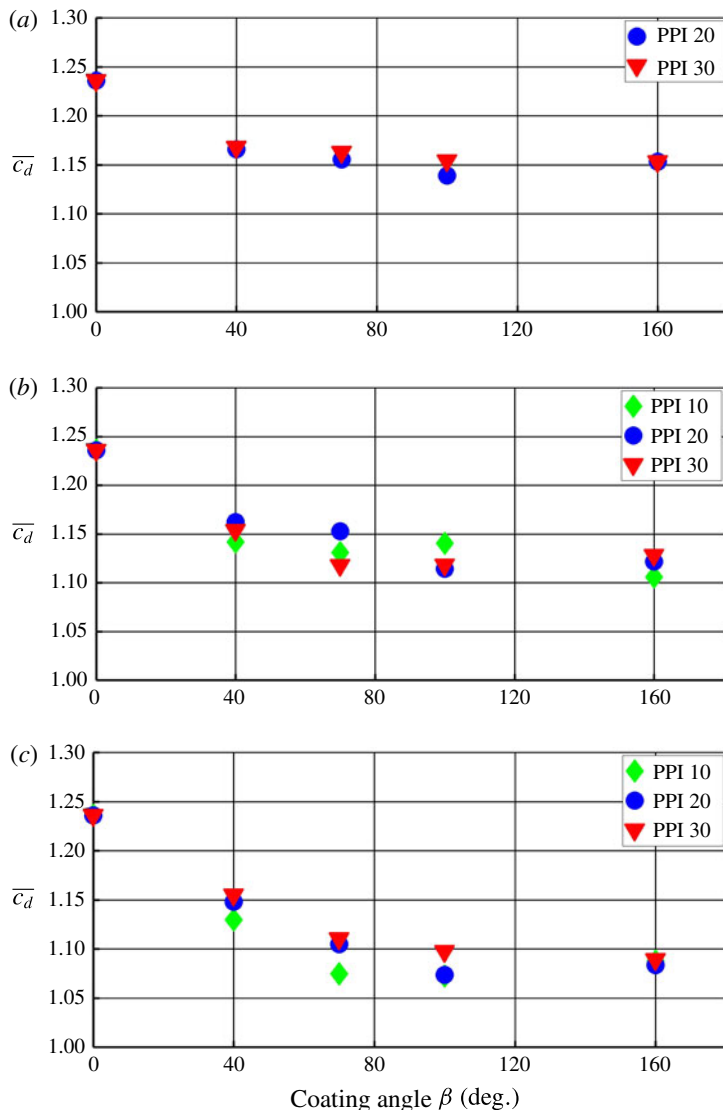


FIGURE 19. (Colour online) Drag coefficient \bar{c}_d with constant layer thickness over varying coating angle (a) $d_M = 3$ mm, (b) $d_M = 5$ mm, (c) $d_M = 10$ mm.

3.3.2. Constant layer thickness with varying coating angle and varying porosity

The results of figure 18 can also be plotted such that layer thickness in each plot is constant, see figure 19(a–c). In these specific plots, it can be seen easily that porosity variation induces a relatively small variation of the drag coefficient \bar{c}_d . The results of layer thickness $d_M = 3$ mm differ slightly only with varying coating angles, see figure 19(a). When compared to figure 19(a), the results of figure 19(b,c) indicate a more effective reduction of \bar{c}_d . Again, it seems that the coating angle of $\beta \geq 100^\circ$ yields the best \bar{c}_d reduction, whereas a coating angle of $\beta = 40^\circ$ causes the smallest reduction of drag coefficient \bar{c}_d . As can be inferred from figure 19(c), for the layer thickness of $d_M = 10$ mm, a significant reduction in \bar{c}_d can be obtained with a coating angle of $\beta = 70^\circ$ already.

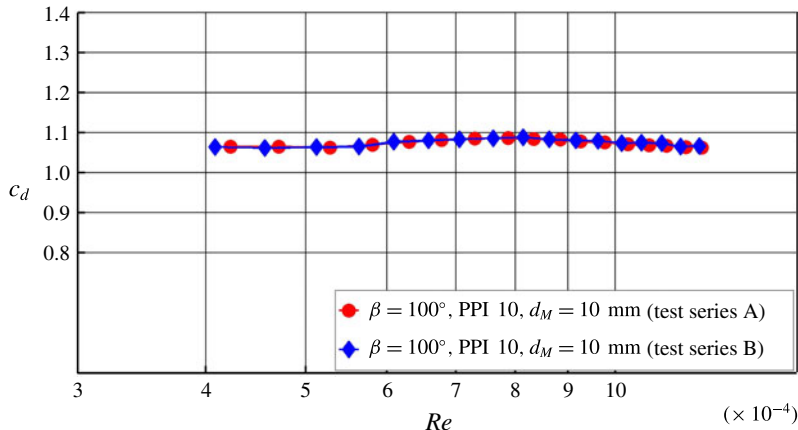


FIGURE 20. (Colour online) Reproducibility of the drag measurements for the cylinder configuration of $\beta = 100^\circ$, PPI 10, $d_M = 10$ mm.

3.4. Reproducibility of the results

In some cases, the measured forces in the wind tunnel differed slightly only. To check whether these small differences can be measured unambiguously and are not subject to a limited measurement accuracy, the reproducibility of the measurements has been investigated. Force measurements for each configuration were repeated on different days during the measurement period. Each time, re-installation in the measuring section was required. Figure 20 shows two examples of drag coefficient measurements performed on different days with newly installed test cylinders of coating angle $\beta = 100^\circ$, porosity PPI 10, and layer thickness $d_M = 10$ mm. The reproducibility of the results was very good and corresponded to a deviation of drag coefficient of less than 0.15 %.

3.5. Influence of leeward porous coating on base pressure

Figure 21 compares the pressure coefficient c_p results for half the circumference of the cylinder with a configuration of $\beta = 100^\circ$, $d_M = 10$ mm and PPI 10 to the results of the reference cylinder. The pressure distributions for both cylinders are almost congruent on the windward side up to a circumferential angle of about $\phi = 60^\circ$. From that point on, pressure around the cylinder with an inserted porous layer increases when compared to the reference cylinder. In the region of the porous layer ($\phi \geq 130^\circ$) an increase of base pressure of up to 29 % is recorded. Apparently, the porous layer on the leeward side of the cylinder also influences the pressure behaviour in the region $\phi \leq 130^\circ$, i.e. upstream of the porous layer. This changed pressure distribution is similar to the upstream pressure change due to a splitter plate in the wake of a cylinder, see Roshko (1955, 1961). Vortex shedding exists also for the configuration $\beta = 100^\circ$, $d_M = 10$ mm. Flow separation occurs for both cylinders with and without porous layers at a circumferential angle of approximately $\phi = 75^\circ$. The separation angle was determined at the location where the root-mean-square value c_{prms} has its maximum, see West & Apelt (1993). The shedding frequency can be seen as a clear peak in the spectrum in figure 22 for the reference cylinder (a) and for the cylinder with a porous layer in the lee (b). Comparing both spectra reveals an increase in shedding frequency from 39.3 Hz to 43.1 Hz, a narrowing of the spectrum

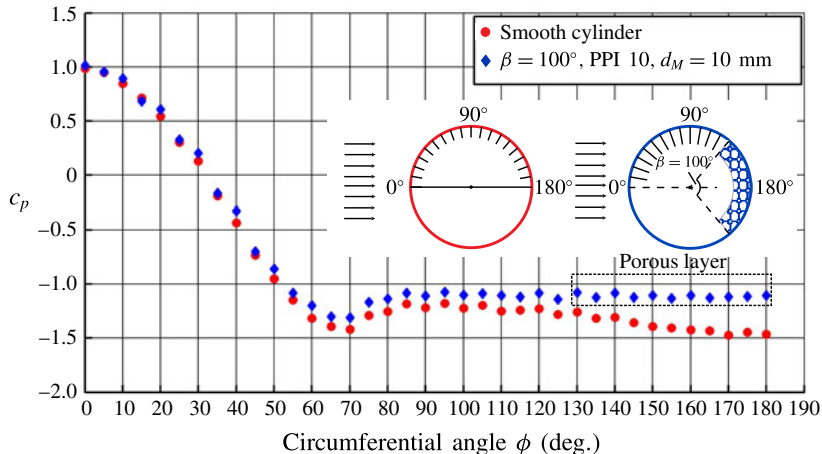


FIGURE 21. (Colour online) Pressure coefficient c_p of the reference cylinder and the cylinder with $\beta = 100^\circ$, PPI 10, $d_M = 10$ mm; $Re = 6.4 \times 10^4$.

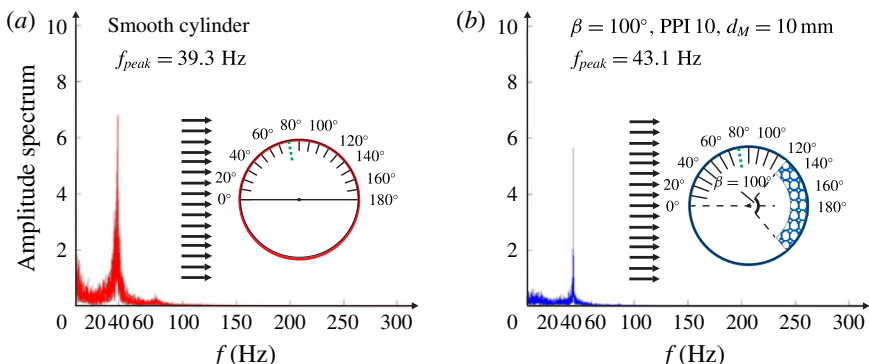


FIGURE 22. (Colour online) Amplitude spectrum of the pressure fluctuations at $\phi = 80^\circ$, (a) smooth cylinder, (b) smooth cylinder with porous layer in the lee ($\beta = 100^\circ$, PPI 10, $d_M = 10$ mm), $Re = 6.4 \times 10^4$.

and a decrease of fluctuations for the cylinder with a porous layer in the lee. The decrease of standard deviation of pressure fluctuations for the cylinder with a porous layer in the lee is shown in detail in figure 23. Due to the significant reduction of pressure fluctuations, the porous layer in the lee of the cylinder obviously leads to a regularization of the flow, which is in accordance with the findings of Price (1956) and Wong (1979).

Figure 24 shows the comparison of the pressure measurements for the taps beneath the porous coating and for the taps that are flush with the porous surface. The results show no difference for the mean pressure coefficient \bar{c}_p . Only very small differences are visible for the standard deviation. The results show that the pressure measurements below the highly porous material used in our experiments are not subject to additional distortion.

3.6. Surface roughness of the porous material

To consider the effect of surface roughness of the foam material and, therefore, to investigate how much the roughness of the porous material contributes to the obtained

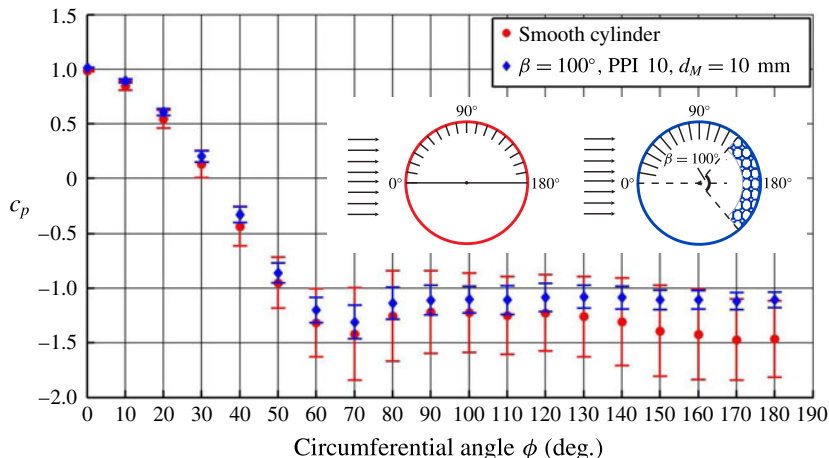


FIGURE 23. (Colour online) Pressure coefficient c_p with standard deviation (bars) for the smooth cylinder and the smooth cylinder with porous layer in the lee ($\beta = 100^\circ$, PPI 10, $d_M = 10$ mm); $Re = 6.4 \times 10^4$.

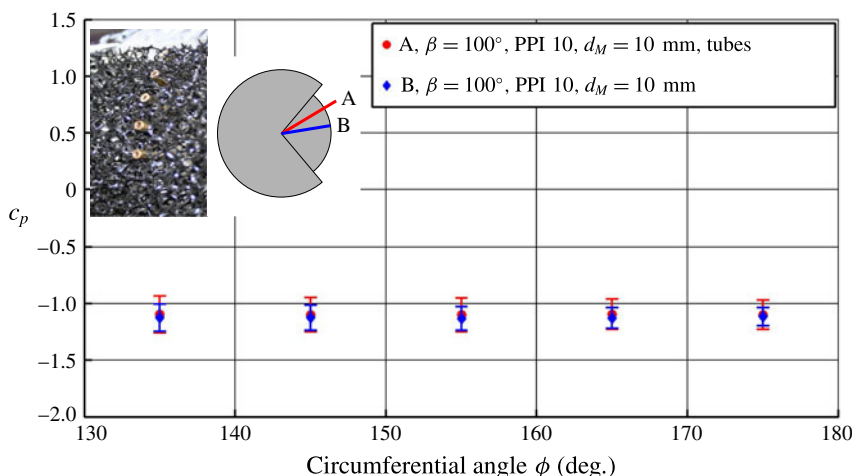


FIGURE 24. (Colour online) Comparison of the signals of pressure taps beneath the porous coating with those which are flush with the coating surface. Mean pressure coefficient and standard deviation (bars) for line 2 of the pressure measurements.

results of this study additional experiments were carried out with foam material PPI 10, which is the material with the highest surface roughness. The mean size of the pore diameter of PPI 10 foam material is $d_{PPI10} = 2.54$ mm. In comparison to a rough surface and therefore to impermeable rough layers, the characteristic property of a porous layer is that fluid can flow through it. If it would be possible to produce the thinnest porous layer of PPI 10 foam material, the pore arrangement must be ideal with one pore next to each other. For that case, the minimum height d_M of the layer would be the pore diameter $d_{PPI10} = 2.54$ mm itself. To satisfy the condition of a flow inside the layer, the assumption of the roughness height h_r must be: $h_r < d_{PPI10}$. Kuznetsov & Becker (2004) recommend a roughness height of a porous medium of half of the pore diameter. This corresponds to $h_r = d_{PPI10}/2$ and is equal to $h_r = 1.27$ mm.

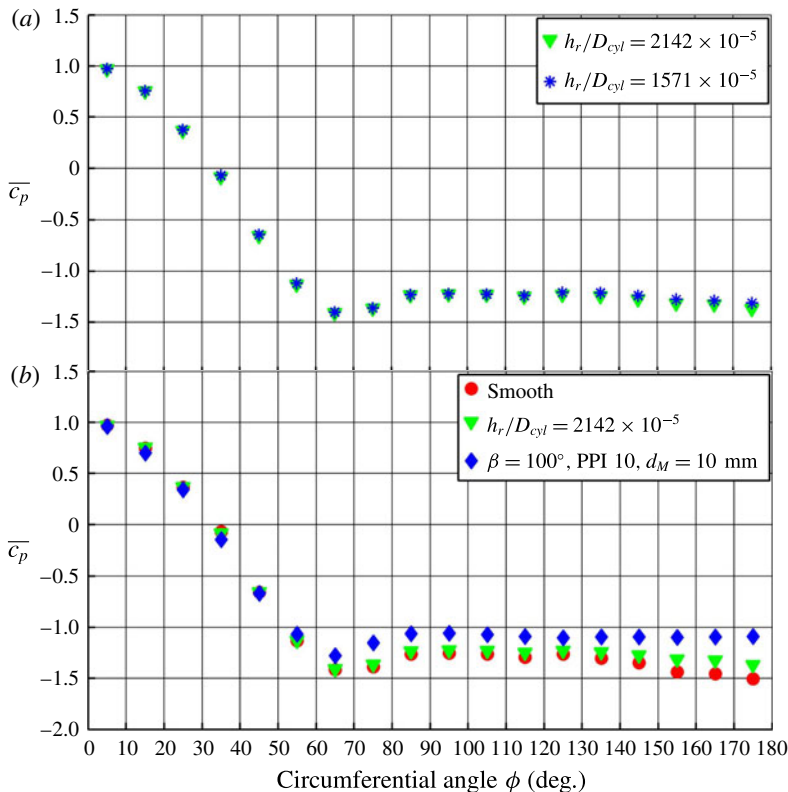


FIGURE 25. (Colour online) Mean pressure distribution around the cylinder. (a) Comparison of the two different emery papers. (b) Comparison of reference cylinder; emery paper $h_r < 1.5$ mm; $\beta = 100^\circ$, PPI 10, $d_M = 10$ mm.

The surface of the PPI 10 material with a roughness height of $h_r = 1.27$ mm is categorized as a very rough surface. The implementation of the rough surface on the leeward side of the cylinder was realized by emery paper which was fixed with a coating angle of $\beta = 100^\circ$ on the reference cylinder. A roughness height of $h_r = 1.1$ mm ($h_r/D_{cyl} = 1571 \times 10^{-5}$) was used. This is the roughest emery paper available in the market. For even rougher conditions, a second self-made emery paper of equal distributed gravel with densest packing was fixed on the cylinder. This corresponds to a roughness height of $1.3 \text{ mm} < h_r \leq 1.5 \text{ mm}$ ($h_r/D_{cyl} = 2142 \times 10^{-5}$).

The two different emery papers deliver only small differences in the mean pressure coefficient, see figure 25(a). Compared to the reference cylinder and to a configuration with an inserted porous layer on the leeward side the pressure plot of the rough cylinder is very similar in shape to the plot of the smooth cylinder with a slightly increased pressure coefficient in the region of the rough surface. Regarding the pressure plot of the configuration with the porous layer, there is an increase even further upstream of the inserted region and an increased c_p in the porous region can be detected, see figure 25(b). The fraction of streamwise pressure force within the modified region (for $\phi > 130^\circ$) is presented in table 4. This shows that pure surface roughness delivers a pressure force reduction of 6.7%, whereas the porous coating leads to a much higher reduction of 18.9%. Thus, increasing surface roughness on

\bar{F}_p (N)	Smooth	Rough leeward surface ($h_r \leq 1.5$ mm, $\beta = 100^\circ$)	Porous leeward coating (PPI 10, $\beta = 100^\circ$)
$\int_{135^\circ}^{175^\circ} (\bar{p} \cos(\phi)) r_0 d\phi$	3.44	3.21	2.79

TABLE 4. Fraction of streamwise pressure force within the modified region for $\phi > 130^\circ$ (for the region of a rough surface and the region of a porous layer) in comparison with the smooth reference cylinder.

the leeward side of a cylinder exerts a certain effect on the drag, but cannot explain alone the measured drag reduction by leeward porous coating.

3.7. Flow field analysis

For a detailed analysis of the flow field around the leeward porous coated cylinder, 2C-2D TR-PIV measurements were performed in the wind tunnel. The turbulence intensity of the flow was less than 1 %. The measurements were carried out at a Reynolds number of $Re = 3 \times 10^4$ characterizing the subcritical range in which a laminar boundary layer and a turbulent wake occur. The measurements were performed with a completely smooth cylinder and a smooth but leeward porous coated cylinder with coating angles of $\beta = 40^\circ$ and $\beta = 100^\circ$. The coating material with porosity PPI 10 and thickness $d_M = 10$ mm was chosen.

Pressure and flow field on the windward side of the cylinders are almost identical. The boundary layers of the cylinders are in laminar state and separation occurs at the same region and seems not to be affected by the leeward coating.

As stated by Zdravkovich (1997), the transition can occur in three different regions around the cylinder (near wake, shear layer, boundary layer) depending on the Reynolds numbers. Increasing the Reynolds number will firstly turn the near wake into turbulent state and, with further increase, the shear layer and, then, after another increase also the boundary layer of the cylinder. Thus, the transition moves in counter-streamwise direction with increasing Reynolds number. In the subcritical case, the near wake is turbulent and the transition takes place in the shear layer. The transition in the shear layer ends when the shear layer is fully turbulent and the transition finally shifts to the boundary layer. Concerning the present study, the region where the leeward porous layer changes the flow conditions compared to the reference cylinder is the shear layer and the near wake.

In figures 26–32 (except figures 29 and 30) the time-averaged data of the PIV measurements for a Reynolds number of $Re = 3 \times 10^4$ are presented. The data are scaled with the approaching flow velocity U . The presented contour plots show the upper half of the field of view due to the symmetric appearance of the flow structure in the near wake.

Considering first the mean velocity components, \bar{u} and \bar{v} , behind the completely smooth and leeward porous coated cylinders, see figure 26, it can be inferred that with increasing coating angle the area of small streamwise and lateral velocity is extended. It can also be seen from figure 26(a) that with increasing coating angle the horizontal free stream velocity outside of the free shear layer protrudes longer into the wake region. The isopatterns of the \bar{u} and \bar{v} component are shifted downstream. This is supported by figure 27, showing a shift of the normal stress pattern in downstream direction and a decrease in strength. At a position $x/D_{cyl} = 0.52$ and $y/D_{cyl} = 0.58$ the streamwise normal stress within the shear layer decreases significantly, from the

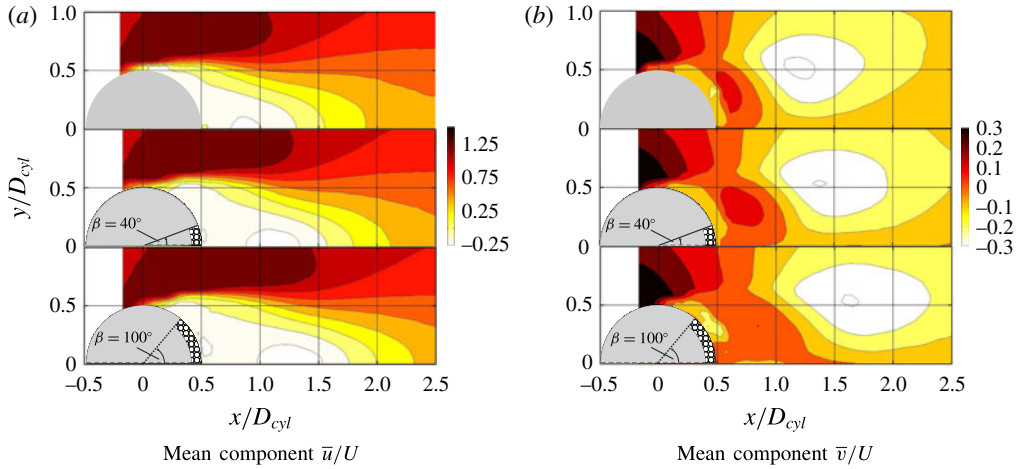


FIGURE 26. (Colour online) Mean velocity components.

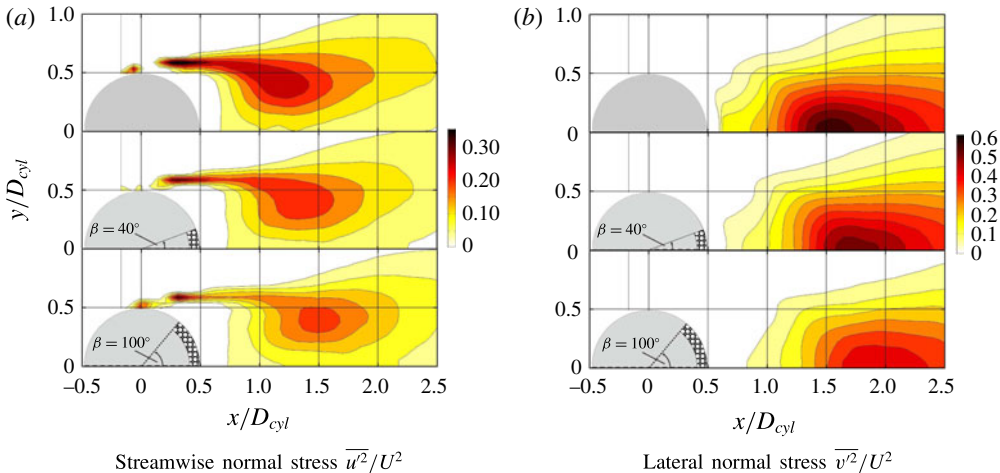


FIGURE 27. (Colour online) Variances of the velocity components.

value 0.33 to 0.19, with increasing coating angle. Figure 28 presents the maximum root-mean-square value of the streamwise component $\sqrt{\bar{u}^2}$ within the shear layer for the smooth cylinder and the configuration $\beta = 100^\circ$, $d_M = 10$ mm, PPI 10. Compared to the smooth cylinder it can be seen that the maximum root-mean-square value of the configuration with a porous layer on the leeward side is reduced in the shear layer at all locations. For $0 < x/D_{cyl} \leq 0.29$ the development is very similar with the same slope for both configurations. The maximum value is reached at $x/D_{cyl} = 0.29$. After that both curves drop until they reach a minimum level. After the minimum the curve slightly rises for the smooth cylinder whereas the curve of the configuration with the porous layer stays more constant on a minimum plateau over several distances x/D_{cyl} before it rises. The porous layer is inserted in the cylinder shape at a location $x/D_{cyl\text{porous}} = 0.32$, which is immediately after the maximum value at the location $x/D_{cyl} = 0.29$. This shows that the porous layer is responsible for a steeper fall of $\sqrt{\bar{u}^2}$.

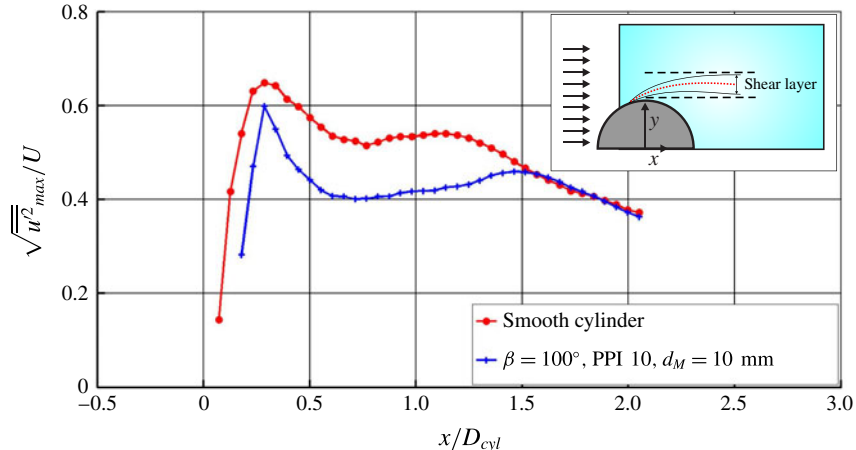


FIGURE 28. (Colour online) Maximum root-mean-square value of the streamwise velocity component $\sqrt{u'^2}$ in the cross-section within the shear layer.

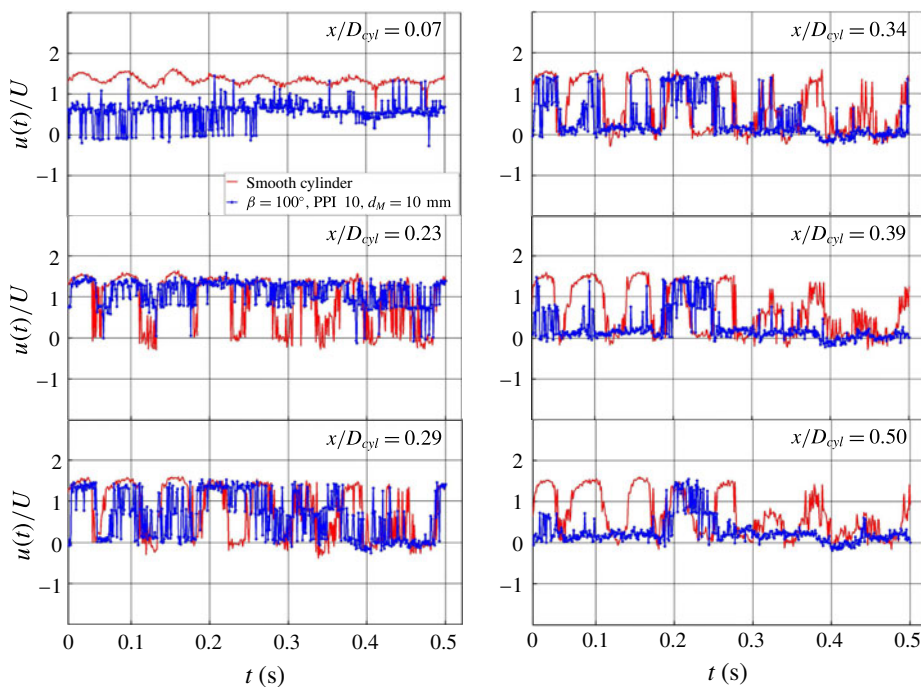


FIGURE 29. (Colour online) Time traces of the horizontal velocity component $u(t)$ within the shear layer at maximum $\sqrt{u'^2}$ locations for the smooth cylinder and the configuration $\beta = 100^\circ$, PPI 10, $d_M = 10$ mm.

Figure 26(b), as well as figure 27(b), indicate that the region of vortex formation is shifted further downstream with increasing coating angle. It is also evident from figures 27(a) and 31(a), that with increasing coating angle the separating free shear layer becomes thinner and, thus, the velocity gradient in the shear layer steepens.

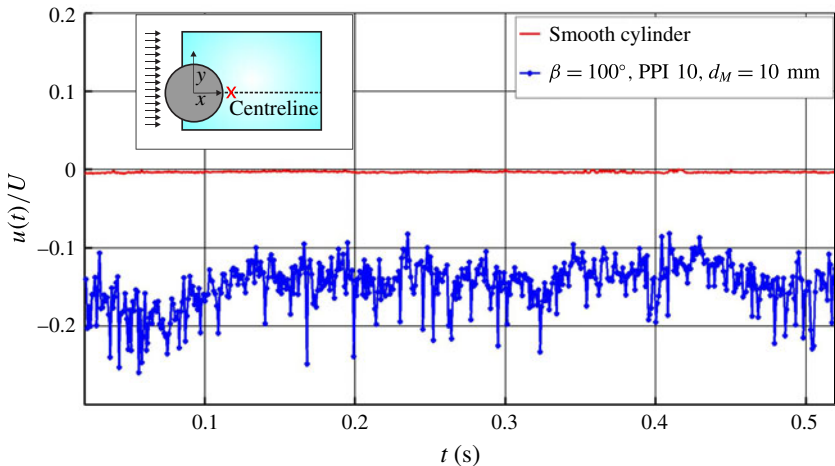


FIGURE 30. (Colour online) Instantaneous streamwise velocity component $u(t)$ at centreline and $x/D_{cyl} = 0.55$.

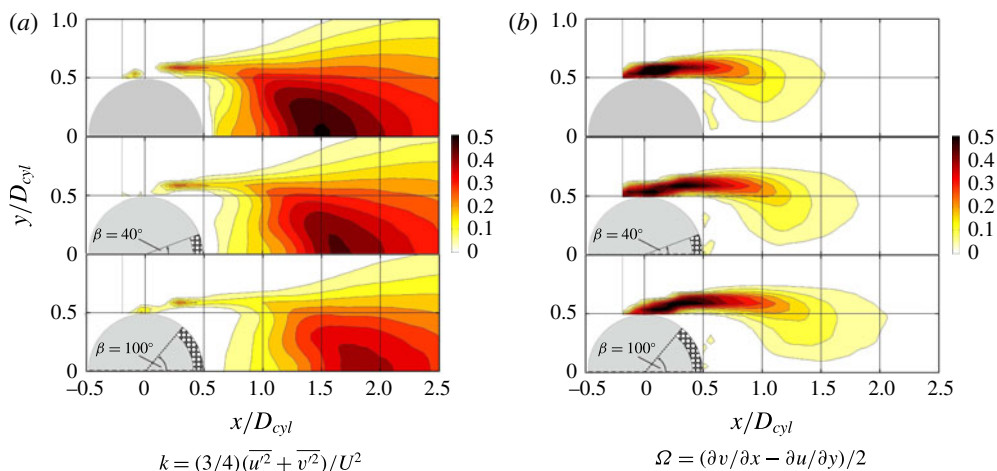


FIGURE 31. (Colour online) Turbulent kinetic energy and vorticity.

Figure 29 presents the time traces of the streamwise component $u(t)$ within the shear layer at different locations x/D_{cyl} where the maximum root-mean-square value appears. At the position $x/D_{cyl} = 0.07$ the plot of the reference cylinder is in good agreement with the results of Bloor (1964). It indicates a regular sinusoidal structure of the time trace before it starts to decompose ($x/D_{cyl} \geq 0.23$). This is immediately before the transition in the shear layer begins. The time traces of the configuration with a porous layer on the leeward side shows a more random signal from the beginning and no typical sinusoidal structures can be found. The fluctuations start to grow until $x/D_{cyl} = 0.29$. At that position both signals show the same strength in fluctuations. After that point and when the location of the porous layer starts ($x/D_{cyl} > 0.29$) the fluctuations decrease whereas the fluctuations of the reference cylinder remain on the same high level as before.

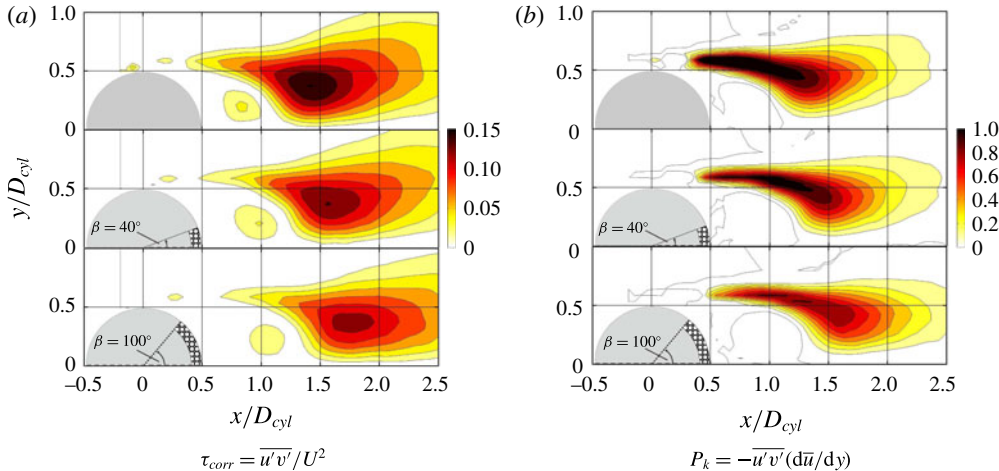


FIGURE 32. (Colour online) Shear stress and production term of turbulent kinetic energy.

Figure 30 displays the time traces for the streamwise component $u(t)$ at the centreline and close to the porous layer at $x/D_{cyl} = 0.55$. It can be inferred that a certain backflow into the porous layer is measured, whereas the streamwise component $u(t)$ of the reference cylinder remains zero at the same position. Considering figure 31(a), we can conclude that a porous layer on the leeward side of a cylinder reduces the turbulent kinetic energy in the free shear layer. Turbulent kinetic energy in the free shear layer decreases with increasing coating angle. The level of turbulent kinetic energy in the near wake decreases from the value $k = 0.5$ for the smooth cylinder to $k = 0.4$ for the configuration with the coating angle $\beta = 100^\circ$. As can be seen from figure 31(b), the vorticity in the shear layer seems to be maintained longer on a high level as in the case of the completely smooth cylinder. In figure 32, the shear stress τ_{corr} and the production term of turbulent kinetic energy P_k is shown. Also, these results show a shift of the isopattern in downstream direction and a decrease in value with increasing coating angle. As can be inferred from figure 22, the vortex shedding frequency is increased by leeward porous coating and figures 27(a), 31(a) and 32(a) indicate that the width of the wake is reduced. This is in agreement with results of Roshko (1954, 1955), who found that in the wake of bluff bodies a universal Strouhal number, $St = 0.16$, occurs when it is formed with the width of the wake instead of the width of the body. In other words, this means for the defined bluff body, that the shedding frequency increases when the width of the wake is reduced as it is the case for leeward coated cylinders.

The vortex street formation is delayed, i.e. shifted downstream, indicating a reduced mixing in the wake. This can be attributed to the increase in base pressure leading to a decrease in pressure fluctuations and a weakened vortex shedding.

3.8. Conclusion

It was shown experimentally that in the measured velocity range defined by $3 \times 10^4 \leq Re \leq 1.4 \times 10^5$ coating by thin porous layers in the lee of smooth cylinders leads to drag reduction. Drag reduction was found for cylinders with porous layers applied to the surface and for porous layers integrated into the cylinder shape. The results indicate that for all variations of layer thickness, coating angle and pore

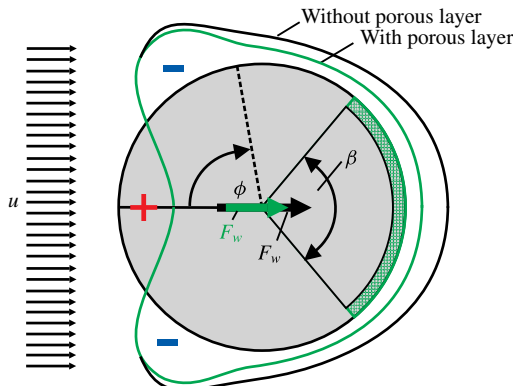


FIGURE 33. (Colour online) Schematic diagram of the increase of time-averaged base pressure resulting in a drag reduction due to a porous layer on the leeward side of a cylinder.

size, a reduction in drag is obtained compared to the reference case of an entirely smooth cylinder. The variation of layer thickness and coating angle exerts a stronger influence on the drag reduction than the pore size variation of the porous material used (96%–99% void fraction). Since the curve of the drag coefficient was almost constant in the considered Reynolds number range, a Re -averaged drag coefficient was introduced. It allowed easy comparisons of the results of many measurement series as a function of the key parameters of coating angle, porous layer thickness, and degree of porosity. The results of the measurements show that for the cylinder tested, leeward porous coating leads to a drag reduction of 7.7%–13.2%. For the varied coating angles, $\beta \geq 100^\circ$ turned out to yield the best drag reduction.

The flow analysis showed that recirculation is still present in the near wake of a leeward coated cylinder, however, the recirculation velocity is decreased when compared to a fully smooth cylinder flow. Pressure measurements around the cylinder reveal that the base pressure is increased by leeward porous coating starting at a circumferential angle of approximately $\phi = 60^\circ$ up to its maximum at $\phi = 180^\circ$ (base of cylinder), as sketched in figure 33. The porous coating weakens the vortex shedding and the rolling up of the free shear layer and, thus, the vortex street formation occurs further downstream from the cylinder and the base pressure increases. The findings are in accordance with those of Galbraith (1980), who concluded that the greater the amount of base bleed is, the longer the vortices take to form and the lower is the drag. Measurements of pressure fluctuations indicate that for leeward coated cylinders, the shedding frequency is increased and a narrower peak in the spectrum occurs. Furthermore, the broadband fluctuations are damped. Leeward porous coating leads to a regularisation of the near wake.

To date, numerical simulations have indicated that porous coating could reduce the drag of bluff bodies up to 45%. The measured reduction rates in our experiments are less than a third of this. Nevertheless, the experimental results shown in this paper confirm qualitatively the numerical results obtained in this field.

The effect of leeward porous coating clearly exists and is worth exploiting technically. The experimental results obtained so far can be used for validation purposes of numerical simulations. The experimental data are indispensable for a realistic formulation of theoretical models and/or the deduction of characteristic

quantities describing the effect of leeward porous coating of bluff bodies. To reach this aim, further experimental investigations are needed and planned with varying cylinder diameters, the objective being to assess the influence of characteristic dimensionless ratios like pore size to cylinder diameter or porous layer thickness to cylinder diameter. Leeward porous coating of bluff bodies seems to be a promising possibility of passive flow control.

4. Summary

Systematic force and pressure measurements were carried out for smooth circular cylinders in wind tunnel cross-flow. The cylinders were coated with a porous layer on the leeward side with varying coating angles, layer thicknesses, and layer porosities. The cylinders had a diameter of 7 cm and a length of 70 cm. Reynolds numbers were in the range of $3 \times 10^4 \leq Re \leq 1.4 \times 10^5$, which corresponds to a velocity range of 6 m s^{-1} to 28 m s^{-1} . All measurement data were compared to data obtained with smooth cylinders without any coating. It was shown by drag force measurements that coating of cylinders in the lee reduced the drag for all tested configurations of cylinder and porous layer. Apparently, drag is reduced irrespective of whether the porous layer is applied to the surface or integrated into the shape of the body. Quantitatively, leeward porous coating led to drag reduction of test cylinders of the order of 7.7%–13.2% depending mainly on layer thickness and coating angle. Furthermore, it was found that the thicker the layer is, the better is the drag reduction. Only small differences in drag reduction could be found for varying layer porosities, which reveals that the degree of porosity of the leeward layer seems to have not the strongest influence. Of the coating angles investigated, optimum coating angles were found at $\beta \geq 100^\circ$. As shown by highly time-resolved force measurements, leeward porous coating reduces oscillations of cylinders. The time-dependent signal of drag force measurement was much more regular and smoother with leeward porous coating. Additionally, it was shown by pressure measurements around the surface of the cylinder that the spectrum of the pressure fluctuations is affected by leeward coating. The characteristic shedding frequency is increased and the broadband fluctuations are reduced significantly. Furthermore, pressure measurements of leeward coated cylinders revealed an increase in base pressure starting at a circumferential angle of about $\phi = 60^\circ$. The maximum was reached at $\phi = 180^\circ$ (base of cylinder). Flow field analyses have shown a decrease of mean velocity components, velocity fluctuations, turbulent kinetic energy and normal stresses in the near wake of a leeward coated cylinder. The beginning of the formation of a regular vortex street is shifted downstream by leeward porous coating.

Acknowledgement

The authors thankfully acknowledge the financial support by the German Research Foundation (DFG research grant no. Ru 345/34-1).

REFERENCES

- ACHENBACH, E. 1971 Influence of surface roughness on the cross-flow around a circular cylinder. *J. Fluid Mech.* **46**, 321–335.
- ACKERET, J. 1926 Grenzschichtabsaugung. *Zeitschrift des VDI* **70** (35), 1153–1158.
- ALLEN, H. J. & VINCENTI, W. G. 1944 Wall interference in a two-dimensional-flow wind tunnel, with consideration effect of compressibility. *NACA* **782**, 155–183.

- BEARMAN, P. W. & HARVEY, J. K. 1993 Control of circular cylinder flow by the use of dimples. *AIAA J.* **31** (10), 1753–1756.
- BEAVERS, G. S. & JOSEPH, D. D. 1967 Boundary conditions at a naturally permeable wall. *J. Fluid Mech.* **30** (01), 197–207.
- BECHERT, D. W. & HOPPE, G. 1985 On the drag reduction of the shark skin. *AIAA Shear Flow Control Conference, AIAA Paper* 85-05.
- BHATTACHARYYA, S. & SINGH, A. K. 2011 Reduction in drag and vortex shedding frequency through porous sheath around a circular cylinder. *Intl J. Numer. Methods Fluids* **65**, 683–698.
- BLOOR, S. 1964 The transition to turbulence in the wake of a circular cylinder. *J. Fluid Mech.* **19** (2), 290.
- BREUGEM, W. P., BOERSMA, B. J. & UITTENBOGAARD, R. E. 2006 The influence of wall permeability on turbulent channel flow. *562*, 35–72.
- BRUNEAU, C.-H. & MORTAZAVI, I. 2006 Control of vortex shedding around a pipe section using a porous sheath. *Intl J. Offshore Polar Engng* **16** (2), 90–96.
- BRUNEAU, C.-H. & MORTAZAVI, I. 2008 Numerical modelling and passive flow control using porous media. *Comput. Fluids* **37** (5), 488–498.
- BRUNEAU, C.-H., MORTAZAVI, I. & GILLIÉRON, P. 2006 Flow regularisation and drag reduction around blunt bodies using porous devices. *European Drag Reduction and Flow Control Meeting, ERCOFATAC*.
- CARBERRY, J., SHERIDAN, J. & ROCKWELL, D. 2005 Controlled oscillations of a cylinder: forces and wake modes. *J. Fluids Struct.* **538** (1), 31.
- CECCIO, S. L. 2010 Friction drag reduction of external flows with bubble and gas injection. *Annu. Rev. Fluid Mech.* **42** (1), 183–203.
- CETINER, O. & ROCKWELL, D. 2001 Streamwise oscillations of a cylinder in steady current. Part 2. Free-surface effects on vortex formation and loading. *J. Fluid Mech.* **427**, 29–59.
- CHOI, H., JEON, W.-P. & KIM, J. 2008 Control of flow over a bluff body. *Annu. Rev. Fluid Mech.* **40** (1), 113–139.
- CHOI, J., JEON, W. P. & CHOI, H. 2006 Mechanism of drag reduction by dimples on a sphere. *Phys. Fluids* **18** (4), 1–5.
- CHOI, K.-S., JUKES, T. & WHALLEY, R. 2011 Turbulent boundary-layer control with plasma actuators. *Phil. Trans. R. Soc. Lond. A* **369** (1940), 1443–1458.
- DALTON, C. 1971 Allen and Vincenti Blockage corrections in a wind tunnel. *AIAA J.* **9** (9), 1864–1865.
- FAGE, A. & WARSAP, J. H. 1929 The effects of turbulence and surface roughness on the drag of a circular cylinder. *Aero. Res. Counc. R&M* 1283, HMSO.
- FRANSSON, J. H. M., KONIECZNY, P. & ALFREDSSON, P. H. 2004 Flow around a porous cylinder subject to continuous suction or blowing. *J. Fluids Struct.* **19** (8), 1031–1048.
- FROHNAPFEL, B., JOVANOVIĆ, J. & DELGADO, A. 2007 Experimental investigations of turbulent drag reduction by surface-embedded grooves. *J. Fluid Mech.* **590**, 107–116.
- GALBRAITH, R. A. 1980 Flow pattern around a shrouded cylinder at $Re = 5 \times 10^3$. *J. Wind Engng Ind. Aerodyn.* **6**, 227–242.
- GALBRAITH, R. A. 1981 Aspects of the flow in the immediate vicinity of a porous shroud. *J. Wind Engng Ind. Aerodyn.* **8**, 251–258.
- HAHN, S., JE, J. & CHOI, H. 2002 Direct numerical simulation of turbulent channel flow with permeable walls. *J. Fluid Mech.* **450**, 259–285.
- HOERNER, S. F. 1965 *Fluid-Dynamic Drag*. Selbstverlag.
- HOYT, J. W. 1972 The effect of additives on fluid friction. *J. Basic Engng* **94** (2), 258–285.
- JAMES, D. F. & TRUONG, Q.-S. 1972 Wind load on cylinder with spanwise protrusion. *J. Engng Mech. ASCE* **98**, 1573–1589.
- VON KÁRMÁN, T. 1911 Über den Mechanismus des Widerstandes den ein bewegter Körper in einer Flüssigkeit erfährt. *Nachrichten von der Gesellschaft der Wissenschaften zu Göttingen, Mathematisch-Physikalische Klasse* **1911**, 509–517.
- KONG, F. Y. & SCHETZ, J. A. 1982 Turbulent boundary layer over porous surfaces with different surface geometries. *AIAA Paper* 82-0030.

- KUZNETSOV, A. V. & BECKER, S. M. 2004 Effect of the interface roughness on turbulent convective heat transfer in a composite porous/fluid duct. *Intl Commun. Heat Mass Transfer* **31** (1), 11–20.
- DE LEMOS, M. J. S. 2005 Turbulent kinetic energy distribution across the interface between a porous medium and a clear region. *Intl Commun. Heat Mass Transfer* **32** (1–2), 107–115.
- DE LEMOS, M. J. S. & SILVA, R. A. 2006 Turbulent flow over a layer of a highly permeable medium simulated with a diffusion-jump model for the interface. *Intl J. Heat Mass Transfer* **49**, 546–556.
- LIN, J., TOWFIGHI, J. & ROCKWELL, D. 1995 Near-wake of a circular cylinder: control by steady and unsteady surface injection. *J. Fluids Struct.* **9**, 659–669.
- LUMLEY, L. 1969 Drag reduction by additives. *Annu. Rev. Fluid Mech.* **1**, 367–387.
- MASKELL, E. C. 1963 A theory of blockage effects on bluff bodies and stalled wings in a closed wind tunnel. *Aero. Res. Counc. R&M* 3400, HMSO.
- MERKLE, C. L. & DEUTSCH, S. 1992 Microbubble drag reduction in liquid turbulent boundary layers. *Appl. Mech. Rev.* **45** (3), 103–127.
- MOESSNER, M. & RADESPIEL, R. 2015 Modelling of turbulent flow over porous media using a volume averaging approach and a Reynolds stress model. *Comput. Fluids* **108**, 25–42.
- MOREAU, E. 2007 Airflow control by non-thermal plasma actuators. *J. Phys. D* **40** (3), 605–636.
- PERLIN, M. & CECCIO, S. 2015 *Mitigation of Hydrodynamics Resistance*, 1st edn. World Scientific.
- PRICE, P. 1956 Suppression of the fluid-induced vibration of circular cylinders. *J. Engng Mech. ASCE* **82** (3), 1–22.
- ROSHKO, A. 1954 On the drag and shedding frequency of two-dimensional bluff bodies *NACA TN* 3169.
- ROSHKO, R. 1955 On the wake and drag of bluff bodies. *J. Aero. Sci.* **22** (2), 124–132.
- ROSHKO, R. 1961 Experiments on the flow past a circular cylinder at very high Reynolds number. *J. Fluid Mech.* **10**, 345–356.
- SCHLICHTING, H. 1948 Ein Näherungsverfahren zur Berechnung der laminaren Reibungsschicht mit Absaugung*. *Ingenieur-Archiv* **16** (3), 201–220.
- SHIH, W. C. L., WANG, C., COLES, D. & ROSHKO, A. 1993 Experiments on flow past rough circular cylinders at large Reynolds numbers. *J. Wind Engng Ind. Aerodyn.* **49** (1–3), 351–368.
- STANSBY, P. K. 1974 The effects of end plates on the base pressure coefficient of a circular cylinder. *Aeronaut. J.* **78**, 36–37.
- STROUHAL, V. 1878 Über eine besondere Art der Tonerregung. *Ann. Phys. Chem.* **5** (10), 216–251.
- SZEPESSY, S. 1993 On the control of circular cylinder flow by end plates. *Eur. J. Mech. (B/Fluids)* **12** (2), 217–243.
- VAFAI, K. & THIYAGARAJA, R. 1987 Analysis of flow and heat transfer at the interface region of a porous medium. *Intl J. Heat Mass Transfer* **30** (7), 1391–1405.
- WEST, G. S. & APELT, C. J. 1993 Measurements of fluctuating pressures and forces on a circular cylinder in the Reynolds number range 10^4 to $2,5 \times 10^5$. *J. Fluids Struct.* **7**, 227–244.
- WESTERWEEL, J. & SCARANO, F. 2005 Universal outlier detection for PIV data. *Exp. Fluids* **39**, 1096–1100.
- WIESELSBERGER, C. 1913 Der Luftwiderstand von Kugeln. *Z. Lufttechnik Motorluftschiffahrt* **5**, 140–144.
- WIESELSBERGER, C. 1921 Neuere Feststellungen über die Gesetze des Flüssigkeits- und Luftwiderstandes. *Physik. Z.* **114**, 321–328.
- WONG, H. Y. 1979 A means of controlling bluff body flow separation. *J. Ind. Aerodyn.* **4**, 183–201.
- ZAGNI, A. F. E. & SMITH, K. V. H. 1976 Channel flow over permeable beds of graded spheres. *J. Hydraul. Div. ASCE* **102**, 207–222.
- ZDRAVKOVICH, M. M. 1997 *Flow Around Circular Cylinders. Vol 1: Fundamentals*. Oxford University Press.
- ZDRAVKOVICH, M. M. 2003 *Flow Around Circular Cylinders. Vol 2: Applications*. Oxford University Press.
- ZIPPE, H. J. & GRAF, W. H. 1983 Turbulent boundary-layer flow over permeable and non-permeable rough surfaces. *J. Hydraul. Res.* **21** (1), 51–65.